Industrial Chemistry & Materials

ROYAL SOCIETY OF CHEMISTRY

PAPER

View Article Online
View Journal

Cite this: DOI: 10.1039/d5im00115c

A novel high thermal conductivity powder coating based on synergistic reinforcement of heat conduction and infrared heat radiation

Di Bao,†[abc] Junqi Ning,†[abc] Dan Lin,[abc] Sicheng Yuan,[abc] Jianwen Peng,[abc] Yue Sun,[abc] Huaiyuan Wang, *[abce] Yanji Zhu[d] and Ruitao Wang[e]

Addressing the limitations of conventional organic polymer coatings in thermal management, this study developed an eco-friendly micro-3D expanded graphite powder (MEGP) protection coating that integrates exceptional heat conduction and heat radiation. In terms of thermal conductive filler selection, expanded graphite (EG) with a micro 3D structure was selected as the filler framework of the composite coating, and a self-assembled functional filler (MEG) was obtained after modification with an as-prepared corrosion inhibitor of a Schiff base–Ce complex (SP), which formed a 3D conductive network in the coating by electrostatic self-assembly. The unique architecture endowed MEGP with a remarkable thermal conductivity of 2.6 W m^{-1} K^{-1}, 12-fold higher than that of pure epoxy (common resin for anti-corrosion coatings) and high infrared emissivity (0.95–0.98 at the full spectrum range of 2.5–25 μm), synergistically enhancing heat dissipation through dual conduction and radiation mechanisms. Finite element simulations confirmed superior thermal management performance. Simultaneously, the MEGP coating exhibited robust adhesion (10.4 MPa) and impact resistance (100 cm). Moreover, the impedance modulus of the coating at 0.01 Hz remains above 10^8 Ohm cm^2 during 90 d immersion in a 3.5 wt% NaCl solution, benefiting from the Schiff base–Ce complex. The structure–property relationships between the 3D network architecture and multifunctional performance were elucidated by a systematic study. This novel design provides a new method for preparing functional integrated coatings with high thermal conductivity.

Received 24th June 2025,
Accepted 19th August 2025

DOI: 10.1039/d5im00115c

rsc.li/icm

Keywords: Thermal conductivity; Infrared emissivity; Schiff base; Anti-corrosion; Powder coating.

1 Introduction

Advancements in energy engineering, microelectronics, 5G chips, and advanced battery systems have heightened the structural conflict between escalating thermal flux density and constrained dissipation geometries.[1–3] High thermal accumulation significantly compromises device longevity/stability while posing critical safety thresholds.[4] For heat dissipation, cooling energy systems have experienced a significant rise in applications, which has caused severe energy consumption, carbon emissions, and environmental pollution issues.[5–7] The demand for thermal management is also progressively increasing, which has recently attracted tremendous attention.[8,9] Hence, the critical issue is to develop high-performance thermal management materials to replace energy-intensive cooling methods. Metals are widely used and are ideal heat dissipation materials due to their high thermal conductivity (TC), but metals are prone to corrosion and have low infrared emissivity.[10,11] Differential transformation method (DMT) analysis indicates that higher values of radiation-conduction parameters are desirable when cooling metal fins.[12] The application of polymer-based protective coatings on metal surfaces demonstrates exceptional corrosion inhibition efficacy owing to their operational simplicity, superior substrate compatibility, and exceptional cost-benefit ratio in industrial implementations.[13,14] However, conventional polymer-based protective coatings exhibit inherent limitations in thermal management due to their low thermal conductivity (<0.6 W

[a] School of Chemical Engineering and Technology and State Key Laboratory of Chemical Engineering, Tianjin University, Tianjin 300350, PR China. E-mail: huaiyuanwang@tju.edu.cn
[b] Collaborative Innovation Centre of Chemical Science and Engineering (Tianjin), Tianjin University, Tianjin 300072, PR China
[c] Tianjin Key Laboratory of Chemical process safety and equipment technology, Tianjin 300072, PR China
[d] Tianjin Key Lab Composite & Functional Materials, School of Materials Science and Engineering, Tianjin University, Tianjin 300072, PR China
[e] Zhejiang Institute of Tianjin University, Ningbo 315201, Zhejiang, PR China
† Di Bao and Junqi Ning contribute equally to this work.

m^{-1} K^{-1}).[15] Therefore, it is extremely urgent to develop polymer-based protective coatings with high heat dissipation performance.

Current investigations reveal that systematic studies on polymer-based thermally conductive protective coatings remain scarce.[15] Moreover, carbon-based materials, especially 2D graphene, are mainly employed in polymer-based thermally conductive protective coatings owing to their superior TC, barrier and chemical inertness properties. For example, Liu's group,[16–18] Ding *et al.*,[19] and Zhu *et al.*[20] have systematically investigated and performed in-depth research on the thermal conductivity and anti-corrosion properties of polymer-based thermally conductive protective coatings enhanced by graphene and revealed its strengthening mechanism. The coatings exhibit more than a twofold increase in TC compared with the resin matrix and certain anti-corrosion properties, which proves the positive advantage of graphene in the research on polymer-based thermally conductive protective coatings. However, unlike bulk polymer-based thermally conductive composites, the specificity of the coating preparation process (spraying, scraping, roller coating, *etc.*) does not allow for the pre-construction of a connected filler network structure. The costly graphene can only rely on a large number of physical stacks of 2D lamellae to form a heat transport network with limited TC improvement. In addition, current research predominantly focuses on oil-based coatings, whereas powder-based coatings, which offer distinct advantages, such as virtually zero VOC emissions, high material utilization rates, and environmental friendliness,[21,22] remain significantly understudied.

The axons and dendrites of micro-3D neurons are interconnected *via* synapses to form a 3D network that enables rapid integration, transmission and response to external sensory information.[23,24] Expanded graphite (EG) is a kind of loose and porous worm-like material with a unique micro-3D structure obtained from graphite by intercalation as well as high temperature expansion, and internally connected by graphite/graphene flakes through van der Waals forces.[25,26] EG, as a promising filler, has attracted intensive research interest in thermal management applications owing to its intrinsic high TC, cost-effectiveness, low bulk density, and notable infrared emissivity properties.[27–29] More importantly, a small number of EGs can lap on each other like neurons to form an interpenetrating network structure to enhance heat transfer due to the spatial hindrance effects. Also, the graphite/graphene flakes inside the EG provide a physical barrier effect, while its complex micro-3D connectivity structure can increase the length of the penetration path of corrosive media, resulting in a "labyrinth effect". However, the high electrical conductivity of EG may promote metal corrosion.[30] The excellent electrical conductivity of EG makes it difficult to balance thermal conductivity with corrosion resistance.

Schiff bases (SBs) are compounds added in trace quantities to corrosive environments to suppress the interactions between metals and corrosive media.[31] Their corrosion inhibition efficacy stems from structural features: the –C═N– group enhances the stability of diverse metal systems (steel, aluminum, copper, *etc.*),[32,33] while polar atoms (N, S, *etc.*), unsaturated bonds, and aromatic rings enable electron donation/acceptance. These functional groups facilitate adsorption onto metal surfaces *via* multiple mechanisms, including lone pair electron sharing, π-electron interactions, and electrostatic attraction.[34–36] Additionally, SBs exhibit strong ligand properties, forming stable coordination bonds with various metal ions through their electron-rich active sites.[32] It is well-known that cerium ions have excellent activity inhibition effects, which can enhance the anti-corrosion performance of coatings and reduce metal corrosion.[37,38] However, few studies have focused on the mechanistic role of the Schiff base–Ce complex (SP) in coatings for improving metal corrosion resistance.

In this work, a micro-3D EG modified by the as-prepared Schiff base–Ce complex (MEG) was employed as a functional filler primitive. To maintain its micro-3D structure, epoxy (EP) resin powder was embedded into the MEG micropores *via* capillary forces. Subsequently, the MEGs were interconnected under electrostatic forces during the electrostatic spraying process, forming an interpenetrating network. After curing, the MEGP coating exhibited a wide range of exceptional properties, including a high thermal conductivity (TC) of 2.6 W m^{-1} K^{-1}, excellent infrared emissivity (above 0.95), strong adhesion (over 10 MPa), remarkable impact resistance (no significant cracking or peeling under 100 cm impact) and good anti-corrosion performance (with low-frequency impedance values exceeding 10^8 Ohm cm^2 over 90 d in a 3.5 wt% NaCl solution). Finite element analysis and thermal responsiveness tests further confirmed the superior heat transfer capability of the coating. This study establishes a theoretical foundation for developing thermally conductive protective powder coatings.

2 Results and discussion

2.1 Filler modification of EG

The as-prepared SP was utilized to modify the EG fillers. The micromorphology of EG and MEG fillers was observed using SEM. As shown in Fig. 2a, e and S1, both EG and MEG fillers exhibited a vermicular and porous morphology, which had an apparent micro 3D structure. The EG and MEG fillers exhibited a continuous network structure, which is conducive to constructing 3D networks in coatings in the enlarged view of SEM. The size of MEG was slightly smaller than that of EG fillers, which can be attributed to the mechanical stirring in solution, which induces a slight contraction of pores in EG. In contrast to EG, the TEM image showed the MEG surface had some nanosheets (Fig. 2b and f), and the thickness of MEG increased compared to EG. The surface roughness and microstructure of EG and MEG were tested. The graphite layer surface roughness (Ra) of EG and MEG were 1.21 nm and 1.61 nm, respectively (Fig. 2c and g). The EDS image of

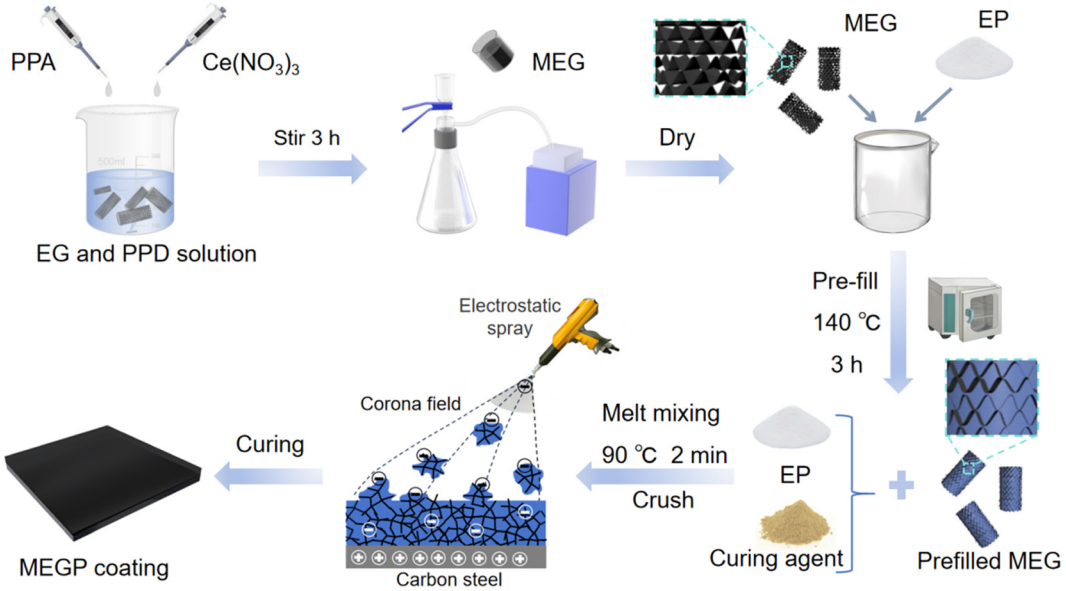

Fig. 1 Schematic of MEGP coating preparation. The composite coating MEGP was prepared through a melt pre-filled process, melt mixing and powder spraying.

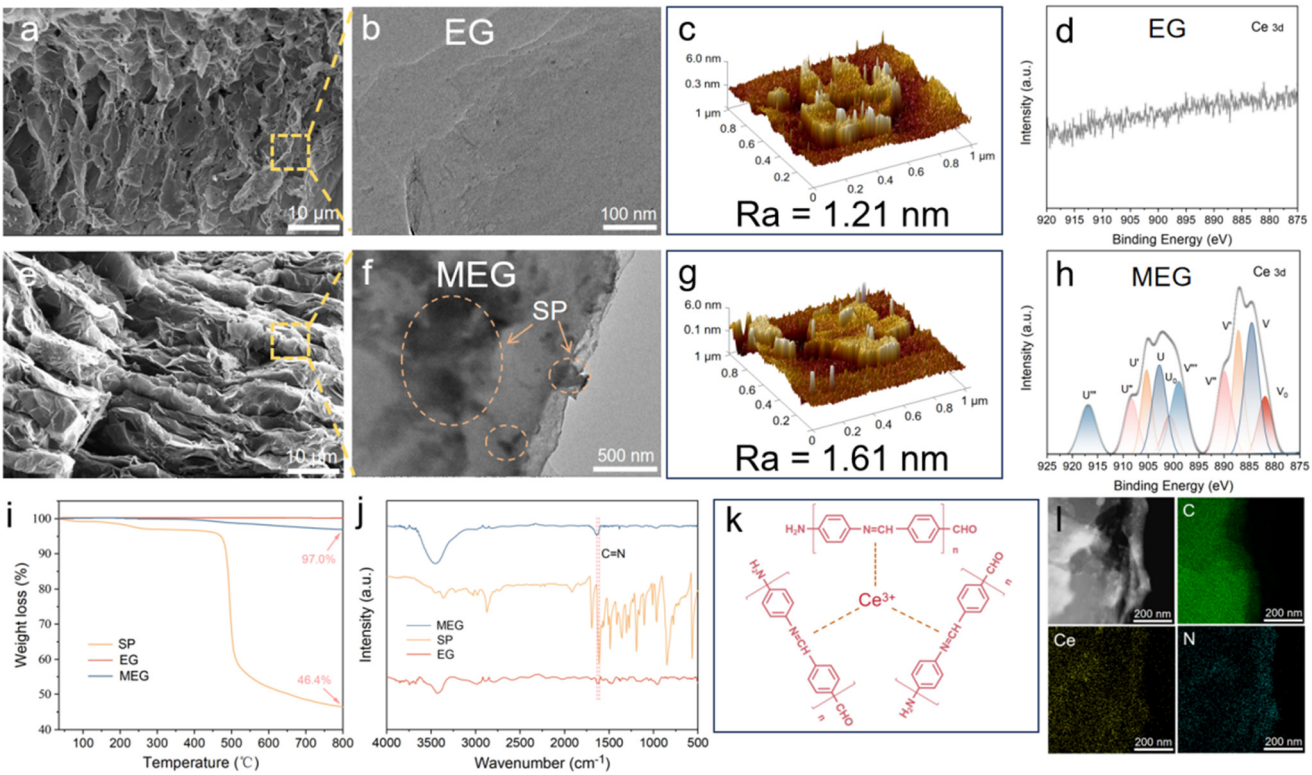

Fig. 2 The SEM, TEM, AFM and XPS images of EG (a–d) and MEG (e–h). TGA (i) and FTIR (j) of SP, EG and MEG. Predicted structures of SP (k). EDS of MEG (l).

MEG (Fig. 2l) demonstrated the elements C, N, and Ce uniformly distributed at the MEG surface. The XPS test is exhibited in Fig. S2–S4 to further analyze the components of EG, SP and MEG. Remarkably, high-resolution spectra of N 1s (Fig. S4) and Ce 3d (Fig. 2d and h) for MEG show apparent characteristic peaks compared with EG (the detailed analysis is shown in the SI). To ensure the thermal stability and content of SP in MEG, the thermal gravimetric analyzer (TGA) was utilized to test the mass change of EG, SP, and MEG from 35 °C to 800 °C. As can be seen in Fig. 2i, the SP started

largely decomposing at about 460 °C and the residual mass of SP was 46.4% at 800 °C. Compared to EG, the mass almost remained unchanged; however, the MEG exhibited an apparent mass change of over 400 °C, which can be attributed to the decomposition of SP. The residual mass of MEG was 97.0%. FTIR was utilized to detect the functional groups of EG, SP, and MEG (Fig. 2j). The characteristic peak at 1611 cm^{-1} in SP can be attributed to the generation of the –C═N– bond.[39,40] The characteristic peak at 1636 cm^{-1} is slightly enhanced in MEG (compared to EG), which may be attributed to the –C═N– bond in SP. The possible structure of the Schiff base–Ce complex is schematically shown in Fig. 2k. The $–NH_2$ in *p*-phenylenediamine (PPD) and –CHO in *p*-phthaldialdehyde (PPA) underwent a condensation reaction, which formed the (–C═N–) functional group. The strong ligand properties of the Schiff base could form stable coordination bonds with the cerium ion through its electron-rich active sites.[41,42] In conclusion, the above results confirmed the presence of SP on the EG surface.

2.2 Morphology of EGP and MEGP coatings

To retain the 3D structure in subsequent operations, the EG and MEG were pre-filled with molten state EP by capillary forces. The morphologies of EG and MEG pre-filled EP are shown in Fig. S5a and d. As can be seen, both EG and MEG maintained the inherent 3D microstructure and the porous structure already filled by EP. To obtain the morphology of EGP and MEGP coatings with different filler contents, the SEM was utilized to observe the section of the coatings. As shown in Fig. 3a and b, S5b and c, the filler networks in the EGP coatings gradually became compact due to the increase in filler content. However, when the filler content reached 9 wt%, the EGP-9 had poor film-forming properties, and the large defects and holes (>200 μm) could be easily observed in the section of the EGP-9 coating (Fig. 3c). For the MEGP coatings (Fig. 3d–i, S5e and f), the filler networks also gradually became compact with the increasing filler content. It is worth noting that MEGP-9 exhibited good film-forming properties, and no apparent defects/holes were observed in the section SEM image. The improved film-forming property of the coatings can be explained by the filler modification that enhanced the interfacial compatibility between the EG filler and the epoxy resin. For the purpose of quantifying the densification degree of the coating, the porosity tests were carried out by mercury injection to test the porosity of EGP and MEGP coatings (Fig. S6). Notably, the porosity of the EGP-9 coating was much higher than that of the MEGP-9 coating, consistent with the surface SEM image of the above coatings, indicating that the MEGP-9 coatings exhibit a more compact surface than the EGP-9 coating.

The high magnification SEM image was utilized to observe the microstructure of the coatings. As shown in Fig. S7a and b, the EDS image exhibits a uniform distribution of C, N, O, and Ce, demonstrating that the MEG was dispersed evenly in the coating. To contrast the formation of the internal thermal conductivity network in coatings, SEM section images of MEGP, GrP (graphene as filler), and CNTP (CNT as filler) coatings are shown in Fig. S8. As can be observed, the EG filler penetrating the resin matrix formed a continuous 3D

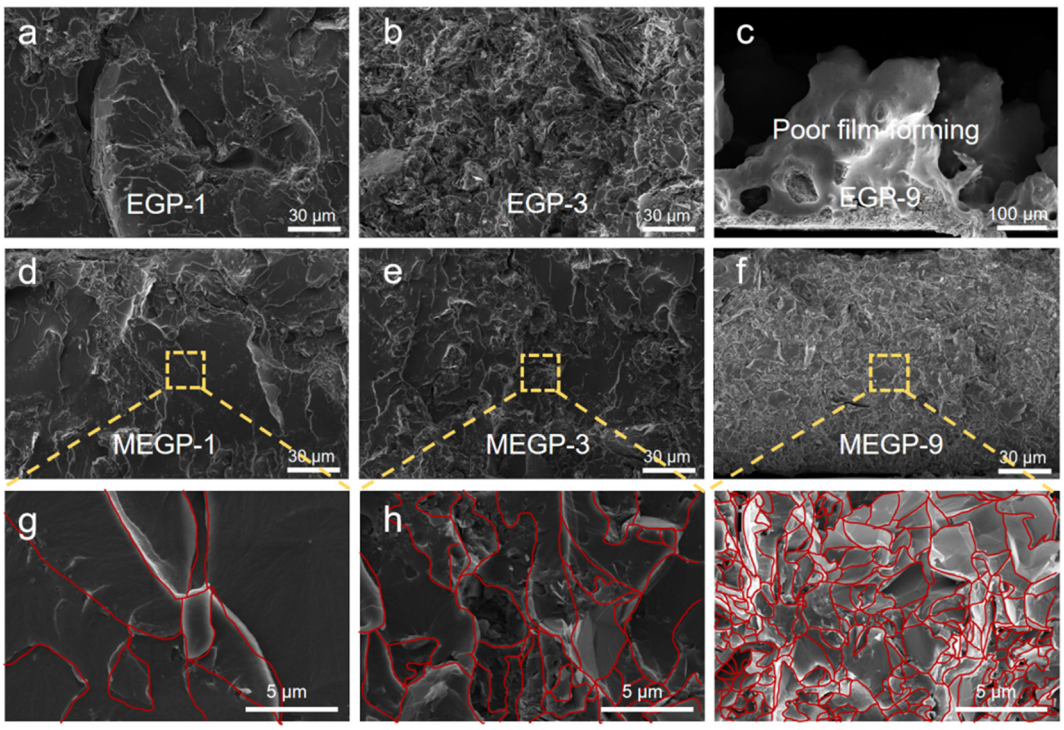

Fig. 3 Morphology of coatings: SEM section images of EGP (a–c) and MEGP (d–i) with different filler contents.

network structure in the MEGP coating, which constructs a continuous phonon transmission path. However, there is no apparent network structure in GrP and CNTP coatings, demonstrating that the 3D carbon filler of EG is more conducive to constructing thermal conduction pathways in the composite coatings at low filler contents.

2.3 Thermal conductivity and infrared emissivity of the coatings

The thermal performance of the coatings is one of the most significant parts of this research. A laser thermal instrument was utilized to test the through-plane TC of coatings. The TC of EGP and MEGP (SP-100) coatings with different filler contents (1, 3, 5, 7, and 9 wt%) are shown in Fig. 4a. The TC of EGP coatings with 1, 3, 5, and 7 wt% filler content were 0.5, 0.7, 1.1, and 1.4 W m^{-1} K^{-1}, respectively. As demonstrated by SEM (Fig. 3c), the EGP-9 coating was unable to form a uniform film and its TC properties could hardly be tested further. The TC of MEGP coatings with 1, 3, 5, 7, and 9 wt% filler contents were 0.4, 0.6, 0.9, 1.3 and 2.6 W m^{-1} K^{-1}, respectively. The TC of MEGP coating with SP-100 is slightly lower than the EGP coatings at the same filler content (1–7 wt%), which might be due to the volume reduction after EG modification. However, the MEGP-9 coating exhibits excellent TC, which is far superior to EGP-9, which is unable to form a film. It is worth emphasizing that the loss of heat transfer coefficient of coated heat exchangers has been reported to be reduced significantly from 9.5% to 1.4% when the TC value of the coating is increased from 0.2 W m^{-1} K^{-1} (pure epoxy coating) to 1.6 W m^{-1} K^{-1}, according to theoretical calculations.[15] Therefore, MEGP-9 coatings with high TC has potential applications in the heat exchanger field.

Moreover, the TC of MEGP-7 coatings with different Schiff base contents was obtained as well. As shown in Fig. 4b, the TC of MEGP-7 coatings increased and then decreased with the addition of SP, and SP-100 was determined as the optimal amount to be used, which indicates that the introduction of SP has a specific role in promoting the improvement of TC. This may be due to the fact that the appropriate amount of

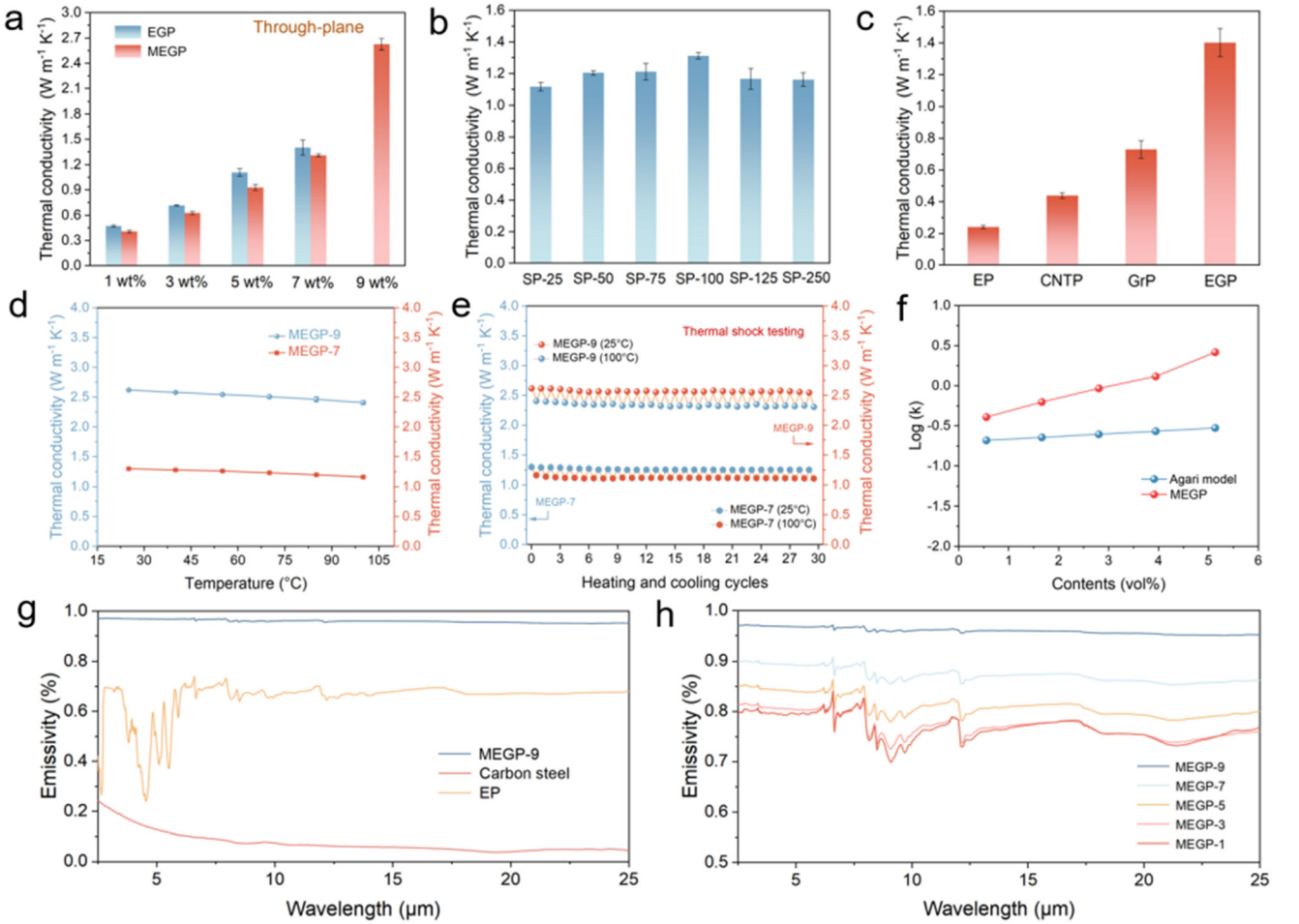

Fig. 4 Thermal conductivity of the coatings: (a) TC of EGP and MEGP coatings with different filler contents. (b) TC of MEGP-7 coatings with different SP contents. (c) TC of the coatings with the fillers of CNTs, Gr and EG at the same filler content. (d) TC of EGP and MEGP coatings at different temperatures. (e) Thermal shock testing of EGP and MEGP coatings. (f) Agari model of MEGP coatings with different filler contents. (g) Infrared emissivity of EP, carbon steel and MEGP-9 coatings. (h) Infrared emissivity of MEGP coatings with different filler contents.

SP strengthened the interfacial compatibility between EG and the epoxy resin. For comparison, different carbon fillers (Gr, CNT, and EG) were utilized to prepare the coatings at 7 wt% filler content. As shown in Fig. 4c, the EGP coatings exhibited the highest TC of 1.4 W m^{-1} K^{-1}, which is much higher than the GrP (0.7 W m^{-1} K^{-1}) and CNTP (0.4 W m^{-1} K^{-1}) coatings at the same filler content. Compared to pure epoxy (0.2 W m^{-1} K^{-1}), the enhancement of TC was 600%, 250%, and 100%, respectively. Furthermore, compared to pure EP, the enhancement for MEGP-9 reached 1200%. The result showed the apparent advantage of EG in constructing a 3D network structure in coatings to improve TC.

Thermal conduction reliability and stability are two essential performance indicators for actual applications. To test the variation of TC as the temperature increases, a laser thermal instrument was utilized to conduct an *in situ* temperature rising test. As shown in Fig. 4d, it is apparent that the TC of both MEGP-7 and MEGP-9 coatings slightly decreased with the increase in temperature, which is consistent with the literature.[43,44] The TC of MEGP-7 and MEGP-9 coatings at 25–100 °C were 1.3–1.1 W m^{-1} K^{-1} and 2.6–2.3 W m^{-1} K^{-1}, respectively. The thermal shock testing during the 30 heating and cooling cycles is shown in Fig. 4e. As can be seen, the TC of MEGP-7 (SP-100) and MEGP-9 coatings (SP-100) remained stable and had less than 5% decrease at 25 °C after the thermal shock test. This result demonstrates that MEGP-7 and MEGP-9 coatings have excellent thermal stability and heat shock resistance. In addition, to determine the internal influencing factors of TC in coatings, the Agari model (Fig. 4f) was used to calculate the theoretical TC (detailed calculation in SI). The result showed that the TC of our MEGP coating was far higher than the theoretical TC value, which demonstrates the formation of 3D network structures in MEGP coatings.

In the heat dissipation process, heat is transferred from the metal to the coating by thermal conduction and then needs to be transferred to the outside air environment by thermal convection and thermal radiation. It is well known that metallic materials, such as carbon steel, are usually low infrared emissivity materials, although they have outstanding TC, which is not conducive to heat dissipation.[11] Therefore, thermal radiation is another essential factor in heat dissipation. The infrared emissivity test was carried out by diffuse reflectance infrared spectroscopy (DRIFTS) from 2.5 μm to 25 μm. As shown in Fig. 4g, the infrared emissivity of the MEGP-9 (SP-100) coating (0.95–0.98) was much higher than that of the pure EP coating (0.2–0.75) and carbon steel (<0.3) with high TC, which had more than 0.95 emissivity at the full spectrum range of 2.5–25 μm. As exhibited in Fig. 4h, the infrared emissivity increased with the increasing filler content. Moreover, we compared the infrared emissivity of commercial heat exchanger coatings and commercial anti-corrosion coatings. The result showed that the infrared emissivity of the MEGP-9 coating is significantly superior to that of the two commercial coatings mentioned above (Fig. S9). Within this system, the primary reason for the high infrared emissivity of MEGP-9 coating is our use of the high-emissivity filler, expanded graphite, and the optimization of the optimal filler loading. On the whole, the MEGP-9 coating combines high TC and high infrared emissivity, which is more efficient than single heat conduction for heat dissipation.

2.4 Heat transfer performance and finite element simulation of the coatings

Aiming to confirm the good thermal transport performance of MEGP coatings, an infrared thermal imaging camera was used to test the surface temperature of the sample when heating or cooling. As shown in Fig. S10, EP, MEGP-9 coatings and pure carbon steel plate (70 mm × 70 mm) were used to contrast the heat transfer performance. As can be seen, the MEGP-9 coating exhibits more rapid heating and cooling speeds than the pure EP coating, which is consistent with TC and infrared emissivity. The surface temperature of the comparison sample, a pure carbon steel plate, cannot be detected by an infrared thermal imaging camera; thus, the thermocouple was utilized to assist in measuring temperature. The EP, MEGP-9 coating, and pure carbon steel plate were all heated to 80 °C and then quickly placed on a table. The coatings were cooled under natural convection conditions, and the thermocouples were used to detect the surface temperature simultaneously. When the temperature detected by the thermocouple begins to drop, the temperature displayed is considered to be the temperature at 0 seconds. As can be seen (Fig. 5a1–a3), the MEGP-9 coating exhibited the most rapid cooling speed compared to the other two samples, which was consistent with the TC and infrared emissivity values.

Aiming to simulate the heat exchanger with water, the carbon steel with/without the coating was made into a container (70 mm × 70 mm × 2 mm) with an open top, and the boiling water (200 g) was poured into the container to test the capacity of heat dissipation (Fig. 5c, S11 and S12). At 7 s, the temperature of water in MEGP-9, EP, and pure carbon steel containers was 87.0, 87.9, and 88.3 °C, respectively. Meanwhile, the container wall temperature of MEGP-9 and EP was 92.4 and 90.0 °C, respectively. This means that MEGP-9 can transfer the heat from the water to the outer walls of the container in a short period of time and at the same time dissipate it through thermal radiation. In short, the container with the MEGP-9-coated carbon steel exhibited the best heat exchange capability, indicating its potential application in heat exchangers.

Finite element simulations of MEGP-9, pure EP, and carbon steel were performed to simulate the heat dissipation of coatings. In the modeling process, the size of the substrate was set to 20 mm × 20 mm × 1 mm, and the thickness of each coating was set to 200 μm. To control the variables, the convective heat transfer and initial temperature of each model were set to be the same. As shown in Fig. 5b1 and S13, all the three models gradually cooled down from 80 °C. The MEGP-9

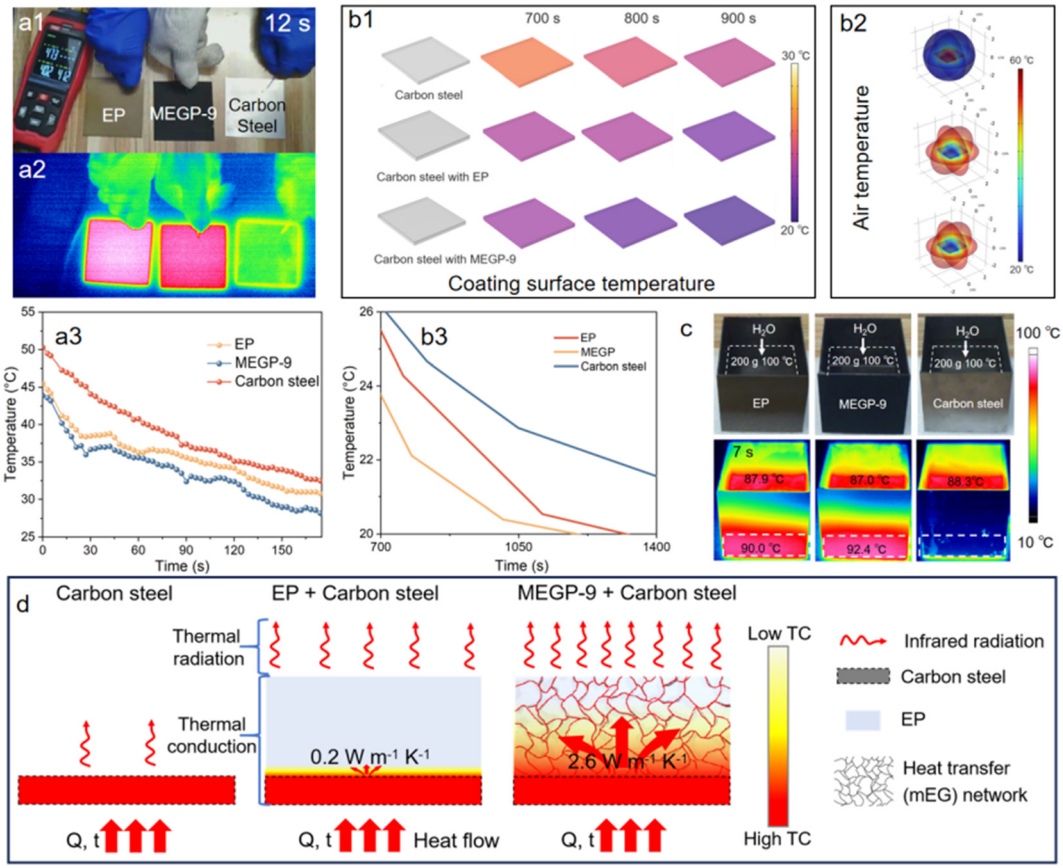

Fig. 5 Heat transfer performance of the coatings. The cooling test image and temperature change curve of EP, carbon steel and MEGP-9 coatings (a1–a3). Finite element simulation of cooling test with EP, carbon steel and MEGP-9 coatings (b1 and b3). Temperature distribution in the air domain around the coatings (b2). Boiling-water cooling experiment and infrared thermography images of EP, carbon steel and MEGP-9 coatings (c). Schematic of the thermal conduction mechanism of the MEGP coating (d).

model exhibited the most rapid rate of heat removal. The surface temperatures of EP, carbon steel and MEGP-9 coatings in finite element simulation are shown in Fig. 5b3 and S14. At 900 s, the surface temperatures of MEGP-9, EP, and pure carbon steel models were about 21.2, 22.7, and 24.0 °C, respectively. Actually, the TC of the carbon steel plate is higher than the MEGP-9 coating, which has a faster heat conduction rate. However, our MEGP-9 coating not only has high TC but also has outstanding infrared radiation performance, which can radiate heat into the air. In Fig. 5b2 and S15, the finite element simulations exhibited the air domain (spherical region) temperature variations for the three models. As can be seen, the carbon steel plate with a coating can radiate more heat into the air than a carbon steel plate without a coating. Under the same energy input, our MEGP-9 coating has a more efficient heat dissipation rate, suggesting that coatings with high infrared emissivity are more conducive to dissipating heat into the air. The simulation results further confirmed the excellent thermal conduction and infrared radiation capability of the MEGP-9 coating, which is expected to be applied in more potential applications in thermal management.

Based on the analysis of the above numerical simulation results, structural characterization, and performance testing, the excellent thermal transport properties of MEGP are mainly attributed to the high TC and infrared emissivity of the coating. As shown in Fig. 5d, for pure carbon steel (high TC + low infrared emissivity), its low infrared emissivity limits radiative heat dissipation into the air, even though heat can be rapidly conducted within it. Also, it is prone to corrosion. For the pure EP coating (low TC + improved infrared emissivity), despite the improved infrared emissivity and anti-corrosion performances, its low intrinsic TC limits the internal heat transfer. With the introduction of the EG with high infrared emissivity heat transfer network into EP, the TC and infrared emissivity of the coating were further enhanced, realizing the enhancement of dual heat dissipation by heat conduction and heat radiation. Meanwhile, the Schiff base–Ce complex inhibits metal corrosion and ultimately obtains a functionally integrated MEGP coating (high TC + high infrared emissivity).

2.5 Corrosion resistance of the coatings

The electrochemical impedance spectroscopy (EIS) measurements were performed to characterize the corrosion

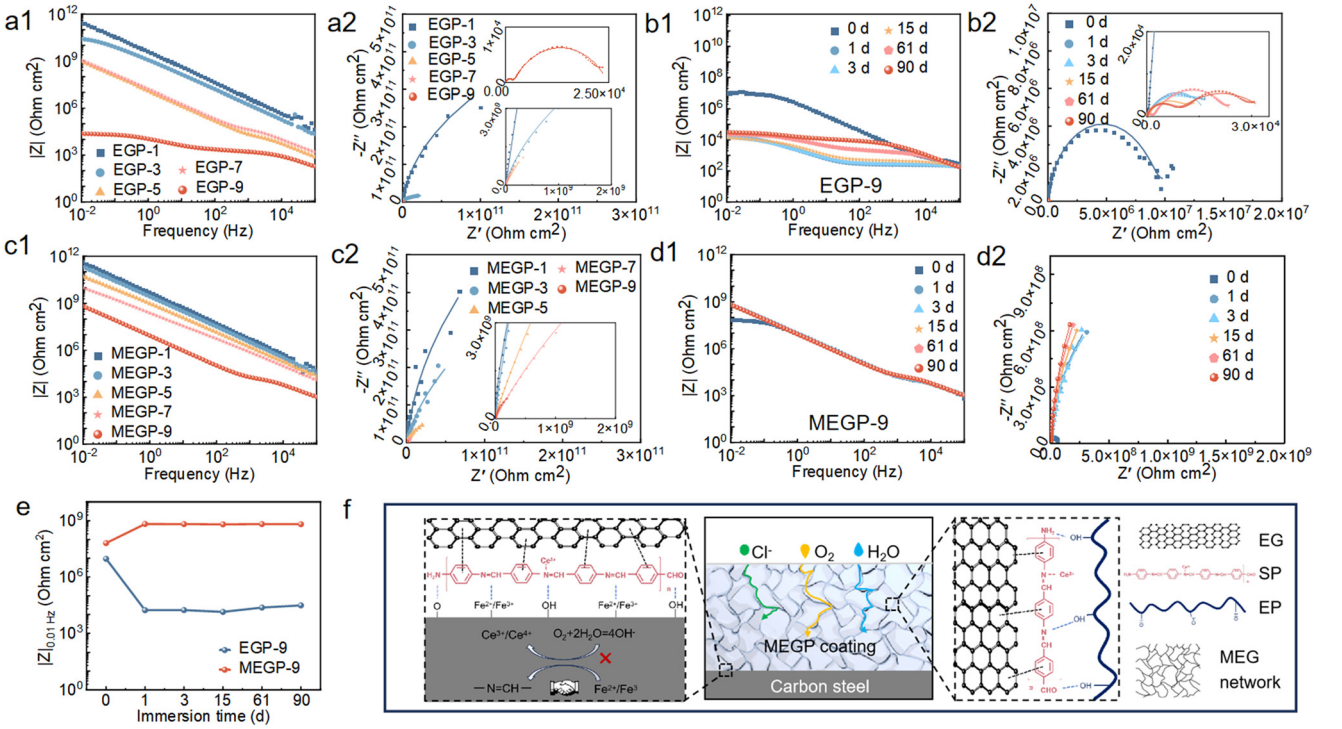

Fig. 6 Bode and Nyquist plots of EGP (a1 and a2) and MEGP (c1 and c2) coatings with different filler contents, and the coatings of EGP-9 (b1 and b2) and MEGP-9 (d1 and d2) with different immersion times. (e) The impedance modulus variation in the coatings with 9 wt% filler loading at 0.01 Hz. Schematic of the anti-corrosion mechanism of the MEGP coating (f).

resistance of the coatings on the carbon steel surface immersed in a 3.5 wt% NaCl solution. In this study, the MEGP coatings with varying filler loadings, Schiff base–Ce complex contents and immersion times were systematically evaluated. Meanwhile, EGP coatings were used for comparison. The results of Bode and Nyquist plots (the equivalent circuit models are illustrated in Fig. S16a and b) are correspondingly illustrated in Fig. 6 and S16. Generally, the low-frequency impedance $|Z|_{0.01Hz}$ in Bode plots characterizes the corrosion protection performance of coatings, with higher values demonstrating a positive correlation with enhanced protective efficacy.[45,46] As the filler addition increased from 1 wt% to 9 wt%, the $|Z|_{0.01Hz}$ value of the EGP coating decreased from 2.7×10^{11} Ohm cm^2 to 2.4×10^4 Ohm cm^2 (Fig. 6a1). Correspondingly, the Nyquist plot demonstrated a reduced capacitive arc radius (Fig. 6a2). The data reveal that the increasing EG content improves TC, but concurrently diminishes corrosion protection. In order to improve thermal conductivity, it is necessary to introduce as much EG/MEG filler as possible to construct a denser heat transfer network. However, as is well known, as the content of the conductive filler increases, a 3D conductive network will form in the coating, which increases the contact between the conductive filler and the metal at the coating defect and enlarges the cathode area in the filler–metal micro-galvanic couple. Therefore, corrosion resistance decreases with increasing EG/MEG content.[30,47,48] It is worth emphasizing that both the $|Z|_{0.01Hz}$ value (4.1×10^{11} to 6.5×10^8 Ohm cm^2) and capacitive arc radius of MEGP coatings after the Schiff base–Ce complex modification were significantly higher than that of the unmodified coatings at the same filler addition amount, indicating that the introduction of the modifier effectively improved the corrosion resistance of the coating (Fig. 6c1 and c2). According to reports, cerium-based materials can protect metal surfaces from corrosion by forming a cerium-rich passivation layer between the corrosive media and metal substrates.[49,50] The –C═N– group in Schiff bases can enhance the stability of carbon steel with various metal systems and slow down corrosion. Additionally, their polar atoms, unsaturated bonds, and aromatic ring structures enable electron donation/acceptance. These functional groups promote adsorption through multiple mechanisms, including lone pair electron sharing, π-electron interactions, and electrostatic attraction.[32–36] Based on this, as shown in Fig. 6f, the polar groups, unsaturated bonds, and aromatic ring structures in SP enhance the interface compatibility between EG and EP, reduce interface defects in the coating, and slow down the penetration of corrosive media. At the same time, the strong bonding between SP and the metal substrate inhibits the corrosion of iron. As a result, the corrosion resistance of the coating is effectively enhanced through SP. We optimized the modifier dosage based on the anti-corrosion properties (Fig. S16d–f), and it can be seen that the optimal dosage is consistent with the TC results (Fig. 4b).

As evidently illustrated in Fig. 6b1, the $|Z|_{0.01Hz}$ value of the EGP-9 coating declined dramatically from around 10^7 Ohm cm^2 to 10^4 Ohm cm^2 after being immersed in NaCl solution for 90 days. Also, the Nyquist plot (Fig. 6b2) showed a reduced capacitive arc radius with increasingly pronounced dual time constants, signifying electrolyte penetration to substrate/coating interfaces and compromised barrier efficiency. Prolonged immersion facilitates direct steel–electrolyte contact, triggering interfacial charge transfer processes. In contrast, the MEGP-9 coating maintained a high $|Z|_{0.01Hz}$ value (>10^8 Ohm cm^2) even after 90 d of saltwater soaking process (Fig. 6d1 and d2). For example, the MEGP-9 coating (6.5×10^8 Ohm cm^2) are four orders of magnitude higher than that of EGP-9 coating (3.1×10^4 Ohm cm^2) on 90 d immersion. In addition, the incomplete capacitive arc radii are larger than those of the EGP-9 coating throughout the entire immersion period for the Nyquist plots, demonstrating good corrosion resistance performance. The impedance modulus variation of EGP and MEGP coatings with 9 wt% filler loading at 0.01 Hz is shown in Fig. 6e. The enhanced corrosion protection capability of the MEGP coating originated from the corrosion inhibition film formed by the Schiff base–Ce complex at the coating-substrate interface and the improved filler–matrix interfacial compatibility (Fig. 6f). In addition, a salt spray test was conducted on MEGP-9 and EGP-9 coatings (Fig. S17). Compared with MEGP-9 coating, EGP-9 coating showed severe corrosion, further proving that the introduction of SP is beneficial to strengthening corrosion resistance.

2.6 Mechanical properties of the coatings

Excellent mechanical properties of coatings are essential for practical applications.[51,52] Adhesion is one of the important properties that indicates the bonding strength between the coating and the carbon steel plate. To evaluate the adhesion strength of the coating, all samples were investigated by a pull-off adhesion tester (Defelsko AT-M) based on the standard of ASTM D4541. Three dollies were glued to the test surface with an adhesive and then cured at room temperature for 72 hours for testing (Fig. 7a). As shown in Fig. 7b, the results showed that the adhesion strength of MEGP coatings was improved compared to EGP coatings. At the same time, almost all MEGP coatings have an adhesion strength of more than 10 MPa and remained at 10.4 MPa for the MEGP-9 coating (only 4.9 MPa for the EGP-9 coating). The reason for the improvement of adhesion strength can be presumed to be the strong ligand properties of the Schiff base–Ce complex. The functional groups of polar N atom, –C═N– unsaturated bond and aromatic ring facilitate adsorption onto carbon steel surfaces by multiple mechanisms, including lone pair electron sharing, π-electron interactions, hydrogen bonding, *etc.* (Fig. 6f). As shown in Fig. 7c, the MEGP coating exhibits good flexibility, which makes it have good plasticity and deformability. Regarding the impact resistance (based on the standard of GB/T 1732-2020), the EGP and MEGP coatings can withstand an impact test of 100 cm (Fig. 7c), which can be attributed to the robust chemical bonds and forces between the resin

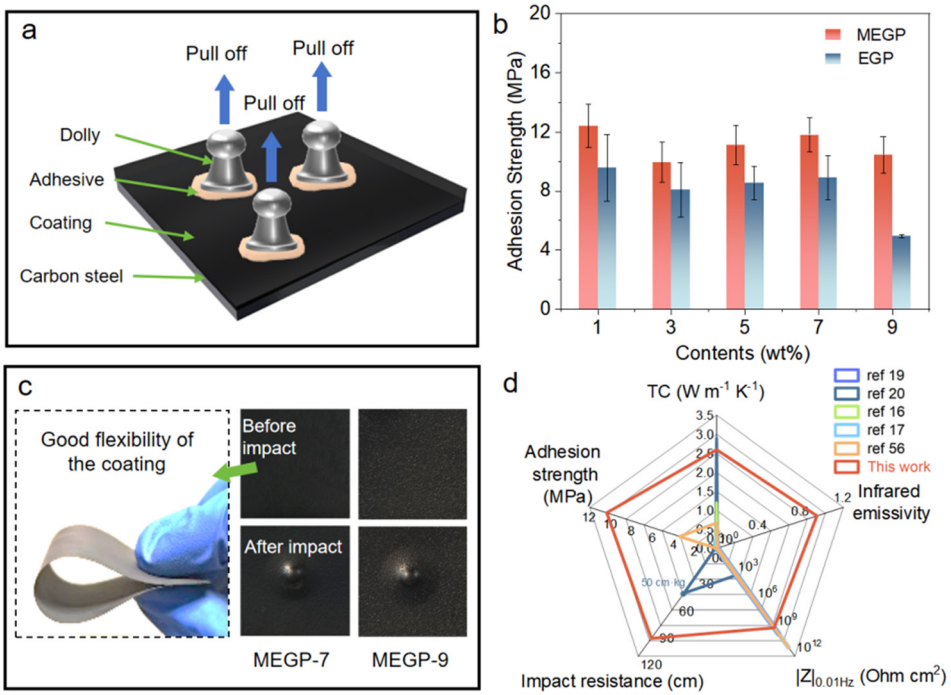

Fig. 7 Mechanical properties and literature comparison of the coatings (a and b) pull-off adhesion and (c) impact resistance test of the coatings. Comparisons of our MEGP-9 coating with some reported carbon-based high TC protective coatings in terms of TC, infrared emissivity, adhesion strength, impact resistance and $|Z|_{0.01Hz}$ performances, where 0 indicates that the corresponding performance was not evaluated in the study (d).

and the substrate, and the addition of modified fillers having good compatibility with the resin. In commercial terms, it is generally considered that the coating has excellent impact resistance, if there are no cracks, wrinkles, or peeling on the coating surface, when the impact height reaches 50 cm.[53–55]

Fig. 7d compared the TC, infrared emissivity, adhesion strength, impact resistance and $|Z|_{0.01Hz}$ performances between our MEGP-9 coating and carbon-based high TC protective coatings in previous reports[16,17,19,20,56] (more details are presented in Table S1). Comparison shows that MEGP-9 coating had an excellent combination of properties. Most of the studies had only explored TC and corrosion protection properties. Our coatings have a TC close to the highest value reported for carbon-based high TC protective coatings, along with good corrosion resistance. In addition, significant adhesion, impact resistance and infrared emissivity were also achieved. This functionally integrated high thermal conductivity coating has potential applications in the field of metal heat dissipation.

3 Conclusions

In this work, an eco-friendly micro-3D expanded graphite powder (MEGP) coating was successfully fabricated, which improves the inherent trade-off between thermal conductivity and corrosion resistance in conventional polymer-based protective coatings. By constructing a 3D network through self-assembled Schiff base–Ce-modified expanded graphite, the MEGP coating achieves dual-functional synergy, exhibiting exceptional thermal conductivity (2.6 W m^{-1} K^{-1}) coupled with high infrared emissivity (0.95–0.98) for efficient heat dissipation, robust adhesion (10.2 MPa), and impact resistance. Finite element simulations further validate its superior thermal management performance. Concurrently, the introduction of the Schiff base–Ce complex ensures corrosion resistance performance, retaining a $|Z|_{0.01Hz}$ value of higher than 10^8 Ohm cm^2 after 90 days of immersion in saline environments. This novel strategy not only mitigates the thermal-conduction limitations of traditional anti-corrosion coatings but also lays a theoretical foundation for scalable applications in energy-efficient material design, demonstrating potential significance in industrial thermal management and marine corrosion protection.

4 Experimental section

4.1 Materials

All chemicals for the experiment were purchased commercially and used as received. EG (80 meshes, volume expansion ratio: 200–300) was purchased from Qing Dao Teng Sheng Da Tan Su Ji Xie Co., Ltd. Cerium nitrate hexahydrate and *p*-phenylenediamine (PPD) were obtained from Shanghai Aladdin Biochemical Technology Co., Ltd. Ethanol absolute was purchased from Tianjin Yuanli Chemical Co., Ltd. (China). Graphene (Gr) and CNT were obtained from Shanghai Titan Scientific Co., Ltd. Sodium chloride and *p*-phthaldialdehyde (PPA) were purchased from Meryer Chemical Technology Co., Ltd. The epoxy resin powder, curing agent, and leveling agent were obtained from Jining Huakai Resin Co., Ltd.

4.2 Filler modification of EG

A specified quality of EG and PPD was dissolved in 300 ml of ethanol and then stirred for about 15 min. The PPA and cerium nitrate hexahydrate were dissolved in 25 ml of ethanol, respectively. The PPA solution and the cerium nitrate solution were added to the EG–PPD mixed solution dropwise. After reacting for 3 h, the SP-modified EG (MEG) was obtained through filtration and drying. PPD : PPA : cerium nitrate = 1 : 1 : 1 (mol : mol : mol). 1 g EG to 25, 50, 75, 100, 125, and 250 × 10^{-6} mol of PPD were named SP-25, SP-50, SP-75, SP-100, SP-125, and SP-250, respectively.

4.3 Pre-filled MEG and preparation of MEGP coating

The molten adsorption method was utilized to pre-fill MEG. Epoxy resin powder was mixed with MEG (the filler content was 30 wt%), and then, molten adsorption was carried out at 140 °C in an oven for 3 h. After that, the epoxy resin, curing agent, pre-filled MEG and leveling agent (0.75 wt%) were mixed in an internal mixer at 90 °C for 2 min. The MEGP-*X* coating was finally obtained by electrostatically spraying and curing (180 °C, 2 h) of the pulverized mixture, where *X* represents the mass fraction of the filler in the coating. The ratio of the resin to curing agent is 15 : 2. For comparison, EGP-*X*, GrP (Gr as filler) and CNTP (CNT as filler) coatings were prepared using the same method. The thickness of the coatings was 150 ± 15 μm. The flowchart of the composite coating preparation process is shown in Fig. 1.

4.4 Characterization

The microstructure, morphology and elemental composition of coatings and fillers were acquired by scanning electron microscopy (SEM, Apreo S LoVac, USA) equipped with an energy dispersive spectrometer (EDS) detector at an acceleration voltage of 5.0 kV. A transmission electron microscope (TEM, JEM-2100F, Japan) at an acceleration voltage of 100 kV was utilized to observe the nanostructure images of EG and MEG fillers. Fourier transform infrared spectroscopy (ATR-FTIR) was performed using an FTIR spectrometer (FT-IR, Perkin-Elmer Spectrum One, USA) with a working range between 4000 and 500 cm^{-1} to investigate EG, SP and MEG. The thermal diffusion performance of composites was evaluated using laser flash analysis (LFA467, Netzsch, Germany). The specific heat capacity of the coatings was obtained by differential scanning calorimetry (DSC 200F3, Netzsch, Germany). The thermal decomposition performance and the content of SP were tested by a thermal gravimetric analyzer (TGA, PerkinElmer TGA 8000, Germany) at a heating rate of 10 °C min^{-1} from 25 to 800 °C under a

nitrogen atmosphere. The surface temperature of the coating with time was tested by an infrared thermograph (Ti480 Pro, Fluke, USA) in the heating and cooling processes. The roughness (Ra) of the filler surface was tested by a portable roughness tester (Mitutoyo, SJ-210). The chemical compositions of EG, SP and MEG were obtained using X-ray photoelectron spectroscopy (XPS, Thermo Scientific K-Alpha). To evaluate the anti-corrosion property of the coatings, electrochemical impedance spectroscopy (EIS) was conducted using an electrochemical workstation (Metrohm Autolab PGSTAT302N) with a conventional three-electrode system in a 3.5 wt% NaCl solution. The infrared emissivity of all coatings was tested by diffuse reflectance infrared spectroscopy (DRIFTS) and the instrument model was Nicolet IS50 with 8 cm^{-1} resolution. All the samples (3 cm × 3 cm) were scanned 128 times in the 2.5–25 um range to obtain the infrared emissivity.

Author contributions

Di Bao: conceptualization, methodology, software, validation, formal analysis, data curation, visualization, writing – original draft, writing – review & editing. Junqi Ning: conceptualization, methodology, software, validation, formal analysis, data curation, visualization, writing – original draft, writing – review & editing. Dan Lin: methodology, validation, writing – review & editing. Sicheng Yuan: writing – review & editing. Jianwen Peng: writing – review & editing. Yue Sun: writing – review & editing. Huaiyuan Wang: conceptualization, funding acquisition, methodology, project administration, resources, supervision, validation, writing – review & editing. Yanji Zhu: supervision, funding acquisition. Ruitao Wang: supervision, funding acquisition.

Conflicts of interest

The authors declare no conflicts of interest.

Data availability

Supplementary information is available. See DOI: **https://doi.org/10.1039/D5IM00115C**.

The data supporting this article have been included as part of the SI. The authors will supply other relevant data in response to reasonable requests.

Acknowledgements

The research is financially supported by the National Natural Science Foundation of China (Grant No. 52303102, 524B2055), the National Science Foundation for Distinguished Young Scholars of China (Grant No. 51925403), the National Key R&D Program of China (2022YFB3808800), the National Natural Science Foundation of China (22378309), Ningbo Science and Technology Innovation 2025 Major Special Project (2022Z112), Ningbo Natural Science Foundation (2022J016), Baima Lake Laboratory Joint Funds of the Zhejiang Provincial Natural Science Foundation of China under Grant No. LBMHZ24E030001.

References

1 Y. Lin, Q. Kang, Y. Liu, Y. Zhu, P. Jiang and Y. Mai, Flexible, highly thermally conductive and electrically insulating phase change materials for advanced thermal management of 5G base stations and thermoelectric generators, *Nano-Micro Lett.*, 2023, **15**, 31.

2 H. Zhao, L. Ran, Y. Xie, F. Sun, L. Yi and L. Zhao, Achieving highly anisotropic thermal and electrical conductivities via synergistic distribution of boron nitride and graphene nanosheets in multilayered composites, *J. Alloys Compd.*, 2023, **935**, 167971.

3 T. Ge, Y. Dai, R. Wang and Z. Peng, Experimental comparison and analysis on silica gel and polymer coated fin-tube heat exchangers, *Energy*, 2010, **35**, 2893–2900.

4 Y. Han, X. Shi, X. Yang, Y. Guo, J. Zhang and J. Kong, Enhanced thermal conductivities of epoxy nanocomposites via incorporating in-situ fabricated hetero-structured SiC-BNNS fillers, *Compos. Sci. Technol.*, 2020, **187**, 107944.

5 L. Geng, T. Xiao, J. Jiang, K. Luo, Y. Yan and C. Liu, Wide temperature range phase change cold energy storage by using esterification between polyethylene glycol and lauric acid, *Chem. Eng. J.*, 2024, **496**, 154005.

6 L. Geng, J. Cui, C. Zhang, Y. Yan, J. Zhao and C. Liu, Chemistry in phase change energy storage: Properties regulation on organic phase change materials by covalent bond modification, *Chem. Eng. J.*, 2024, **495**, 153359.

7 R. Wang, L. Geng, X. Zhang, G. Liang, J. Zhao and C. Liu, Synthesis of flexible form stable phase change materials with in-situ formed porous TiO_2 for personal thermal management, *Chem. Eng. J.*, 2025, **505**, 159592.

8 L. Geng, K. Luo, Y. Lin, G. Li, Y. Cao and J. Zhao, Facile ester-based phase change materials synthesis for enhanced energy storage toward battery thermal management, *Adv. Sci.*, 2025, **12**, 2413703.

9 J. Wang, M. Shen, Z. Liu and W. Wang, MXene materials for advanced thermal management and thermal energy utilization, *Nano Energy*, 2022, **97**, 107177.

10 G. Cui, Z. Bi, R. Zhang, J. Liu, X. Yu and Z. Li, A comprehensive review on graphene-based anti-corrosive coatings, *Chem. Eng. J.*, 2019, **373**, 104–121.

11 S. H. Sadiq, M. B. Wong, J. Tashan, R. Al-Mahaidi and X. Zhao, Determination of steel emissivity for the temperature prediction of structural steel members in fire, *J. Mater. Civ. Eng.*, 2013, **25**, 167–173.

12 A. S. Dogonchi and D. D. Ganji, Convection–radiation heat transfer study of moving fin with temperature-dependent thermal conductivity, heat transfer coefficient and heat generation, *Appl. Therm. Eng.*, 2016, **103**, 705–712.

13 M. Cheng, F. Li, Z. Wang, C. Li, S. Sun and S. Hu, New valve-free organosilica nanocontainer for active anticorrosion of polymer coatings, *Composites, Part B*, 2021, **224**, 109185.

14 H. Chen, H. Fan, N. Su, R. Hong and X. Lu, Highly hydrophobic polyaniline nanoparticles for anti-corrosion epoxy coatings, *Chem. Eng. J.*, 2021, **420**, 130540.
15 F. Xu, M. Zhang, Y. Cui, D. Bao, J. Peng and Y. Gao, A novel polymer composite coating with high thermal conductivity and unique anti-corrosion performance, *Chem. Eng. J.*, 2022, **439**, 135660.
16 Z. Yang, J. Che, Z. Zhang, L. Yu, M. Hu and W. Sun, High-efficiency graphene/epoxy composite coatings with outstanding thermal conductive and anti-corrosion performance, *Composites, Part A*, 2024, **181**, 108152.
17 B. Li, K. Xu, W. Sun, L. Wang, Z. Yang and G. Liu, Beyond graphene: Anticorrosion performance of fluorographene-filled perfluoroalkoxy alkane composite coatings for condensing heat exchanges, *Prog. Org. Coat.*, 2022, **165**, 106748.
18 Z. Yang, S. Yu, W. Sun, Z. Xing, W. Gao and L. Wang, High-efficiency preparation of reduced graphene oxide by a two-step reduction method and its synergistic enhancement of thermally conductive and anticorrosive performance for epoxy coatings, *Ind. Eng. Chem. Res.*, 2022, **61**, 3044–3054.
19 J. Ding, H. Zhao and H. Yu, Bio-inspired multifunctional graphene–epoxy anticorrosion coatings by low-defect engineered graphene, *ACS Nano*, 2022, **16**, 710–720.
20 Q. Shi and A. Zhu, Interface regulation of graphene/carbon nanotube on the thermal conductivity and anticorrosion performance of their nanocomposite, *Prog. Org. Coat.*, 2020, **140**, 105480.
21 X. Zhu, J. Xie, H. Zhang, W. Liu, H. Zhang and J. Zhu, Insights into powder coating excellence: Unveiling the effects of particle-size distribution, *Prog. Org. Coat.*, 2024, **197**, 108815.
22 Z. Du, S. Wen, J. Wang, C. Yin, D. Yu and J. Luo, The review of powder coatings, *J. Mater. Sci. Chem. Eng.*, 2016, **04**, 54–59.
23 C. Sanchez-Priego, R. Hu, L. L. Boshans, M. Lalli, J. A. Janas and S. E. Williams, Mapping cis-regulatory elements in human neurons links psychiatric disease heritability and activity-regulated transcriptional programs, *Cell Rep.*, 2022, **39**, 110877.
24 E.-L. Yap and M. E. Greenberg, Activity-regulated transcription: Bridging the gap between neural activity and behavior, *Neuron*, 2018, **100**, 330–348.
25 S. Wu, T. Li, Z. Tong, J. Chao, T. Zhai and J. Xu, High-performance thermally conductive phase change composites by large-size oriented graphite sheets for scalable thermal energy harvesting, *Adv. Mater.*, 2019, **31**, 1905099.
26 S. Tao, S. Wei and Y. Yulan, Characterization of expanded graphite microstructure and fabrication of composite phase-change material for energy storage, *J. Mater. Civ. Eng.*, 2015, **27**, 04014156.
27 W. Lee and J. Kim, Cellulose nanofiber grafting and aluminum nitride deposition on the surface of expanded graphite to improve the thermal conductivity and mechanical properties of phase change material composites, *Composites, Part B*, 2022, **230**, 109526.
28 Z. Sun, Z. Zhao, Y. Zhang, Y. Li, Y. Fu and B. Sun, Mechanical, tribological and thermal properties of injection molded short carbon fiber/expanded graphite/polyetherimide composites, *Compos. Sci. Technol.*, 2021, **201**, 108498.
29 W. Li, C. Gao, A. Hou, J. Qiu and S. Wang, One-pot in situ synthesis of expandable graphite-encapsulated paraffin composites for thermal energy storage, *Chem. Eng. J.*, 2024, **481**, 148541.
30 W. Sun, T. Wu, L. Wang, Z. Yang, T. Zhu and C. Dong, The role of graphene loading on the corrosion-promotion activity of graphene/epoxy nanocomposite coatings, *Composites, Part B*, 2019, **173**, 106916.
31 P. B. Raja and M. G. Sethuraman, Natural products as corrosion inhibitor for metals in corrosive media — A review, *Mater. Lett.*, 2008, **62**, 113–116.
32 C. Verma and M. A. Quraishi, Recent progresses in Schiff bases as aqueous phase corrosion inhibitors: Design and applications, *Coord. Chem. Rev.*, 2021, **446**, 214105.
33 M. A. Hegazy, A. M. Hasan, M. M. Emara, M. F. Bakr and A. H. Youssef, Evaluating four synthesized Schiff bases as corrosion inhibitors on the carbon steel in 1 M hydrochloric acid, *Corros. Sci.*, 2012, **65**, 67–76.
34 S. Li, S. Lei, H. Ma, R. Yu and D. Liu, Investigation on some Schiff bases as HCl corrosion inhibitors for copper, *Corros. Sci.*, 1999, **41**, 1273–1287.
35 S. Issaadi, T. Douadi, A. Zouaoui, S. Chafaa, M. A. Khan and G. Bouet, Novel thiophene symmetrical Schiff base compounds as corrosion inhibitor for mild steel in acidic media, *Corros. Sci.*, 2011, **53**, 1484–1488.
36 L. Fragoza-Mar, O. Olivares-Xometl, M. A. Domínguez-Aguilar, E. A. Flores, P. Arellanes-Lozada and F. Jiménez-Cruz, Corrosion inhibitor activity of 1,3-diketone malonates for mild steel in aqueous hydrochloric acid solution, *Corros. Sci.*, 2012, **61**, 171–184.
37 B. R. W. Hinton, Corrosion inhibition with rare earth metal salts, *J. Alloys Compd.*, 1992, **180**, 15–25.
38 I. Santana, A. Pepe, E. Jimenez-Pique, S. Pellice, I. Milošev and S. Ceré, Corrosion protection of carbon steel by silica-based hybrid coatings containing cerium salts: Effect of silica nanoparticle content, *Surf. Coat. Technol.*, 2015, **265**, 106–116.
39 Y. Liu, Y. Shi, H. Wang and S. Zhang, Donor–acceptor covalent organic frameworks-confined ultrafine bimetallic Pt-based nanoclusters for enhanced photocatalytic H_2 generation, *Nano Res.*, 2024, **17**, 5835–5844.
40 H. Xu, H. Chen, J. Lv, B. Chen, Z. Zhou and S. Chang, Schiff base reaction in a living cell: In situ synthesis of a hollow covalent organic polymer to regulate biological functions, *Angew. Chem.*, 2023, **62**, e202311002.
41 H. Kargar, M. Fallah-Mehrjardi and K. S. Munawar, Metal complexes incorporating tridentate ONO pyridyl hydrazone Schiff base ligands: Crystal structure, characterization and applications, *Coord. Chem. Rev.*, 2024, **501**, 215587.

42 W. Xie, Y. Liu, Y. Yan, M. Yang, M. Zhang and B. Liu, Metal-mediated Schiff base polymer enables metal/nitrogen codoped carbon nanosheets as efficient bifunctional electrocatalyst for durable rechargeable Zn-air batteries, *Energy Storage Mater.*, 2023, **59**, 102783.
43 W. Dai, X. Ren, Q. Yan, S. Wang, M. Yang and L. Lv, Ultralow interfacial thermal resistance of graphene thermal interface materials with surface metal liquefaction, *Nano-Micro Lett.*, 2022, **15**, 9.
44 Y. Chen, X. Hou, M. Liao, W. Dai, Z. Wang and C. Yan, Constructing a "pea-pod-like" alumina-graphene binary architecture for enhancing thermal conductivity of epoxy composite, *Chem. Eng. J.*, 2020, **381**, 122690.
45 J. Ding, H. Zhao, Y. Zheng, X. Zhao and H. Yu, A long-term anticorrsive coating through graphene passivation, *Carbon*, 2018, **138**, 197–206.
46 J. Ding, O. Rahman, W. Peng, H. Dou and H. Yu, A novel hydroxyl epoxy phosphate monomer enhancing the anticorrosive performance of waterborne graphene/epoxy coatings, *Appl. Surf. Sci.*, 2018, **427**, 981–991.
47 Y. Huang, T. Lo, C. Chao and W. Whang, Anti-corrosion characteristics of polyimide/h-boron nitride composite films with different polymer configurations, *Surf. Coat. Technol.*, 2014, **260**, 113–117.
48 W. Sun, L. Wang, T. Wu, Y. Pan and G. Liu, Inhibited corrosion-promotion activity of graphene encapsulated in nanosized silicon oxide, *J. Mater. Chem. A*, 2015, **3**, 16843–16848.
49 K. An, Y. Sui, Y. Wang, Y. Qing, C. Long and X. Liu, Synergistic control of wetting resistance and corrosion inhibition by cerium to enhance corrosion resistance of superhydrophobic coating, *Colloids Surf., A*, 2022, **653**, 129874.
50 F. Xu, P. Ye, J. Peng, H. Geng, Y. Cui and D. Bao, Cerium methacrylate assisted preparation of highly thermally conductive and anticorrosive multifunctional coatings for heat conduction metals protection, *Nano-Micro Lett.*, 2023, **15**, 201.
51 I. P. Okokpujie, L. K. Tartibu, H. O. Musa-Basheer and A. O. M. Adeoye, Effect of coatings on mechanical, corrosion and tribological properties of industrial materials: A comprehensive review, *J. Bio- Tribo-Corros.*, 2023, **10**, 2.
52 J. Malzbender, J. M. J. den Toonder, A. R. Balkenende and G. de With, Measuring mechanical properties of coatings: a methodology applied to nano-particle-filled sol–gel coatings on glass, *Mater. Sci. Eng., R*, 2002, **36**, 47–103.
53 G. Wu, Z. Kong, J. Chen, S. Huo and G. Liu, Preparation and properties of waterborne polyurethane/epoxy resin composite coating from anionic terpene-based polyol dispersion, *Prog. Org. Coat.*, 2014, **77**, 315–321.
54 J. Ju, Y. Wang, M. Yu, X. Sun, W. Li and Z. Zhao, Anti-corrosion improvement of epoxy coating by the synergistic effect of barrier shielding and slow-release based on phytic acid intercalated hydrotalcite, *J. Appl. Polym. Sci.*, 2023, **140**, e54459.
55 L. Deng, Z. Wang, B. Qu, Y. Liu, W. Qiu and S. Qi, A comparative study on the properties of rosin-based epoxy resins with different flexible chains, *Polymer*, 2023, **15**, 4246.
56 W. Ma, W. Cong, L. Guo, J. Wang, L. Cui and X. Sun, Preparation of thermally conductive and anti-corrosion coating by the insulation modification on graphite, *Ceram. Int.*, 2025, **51**, 2411–2419.